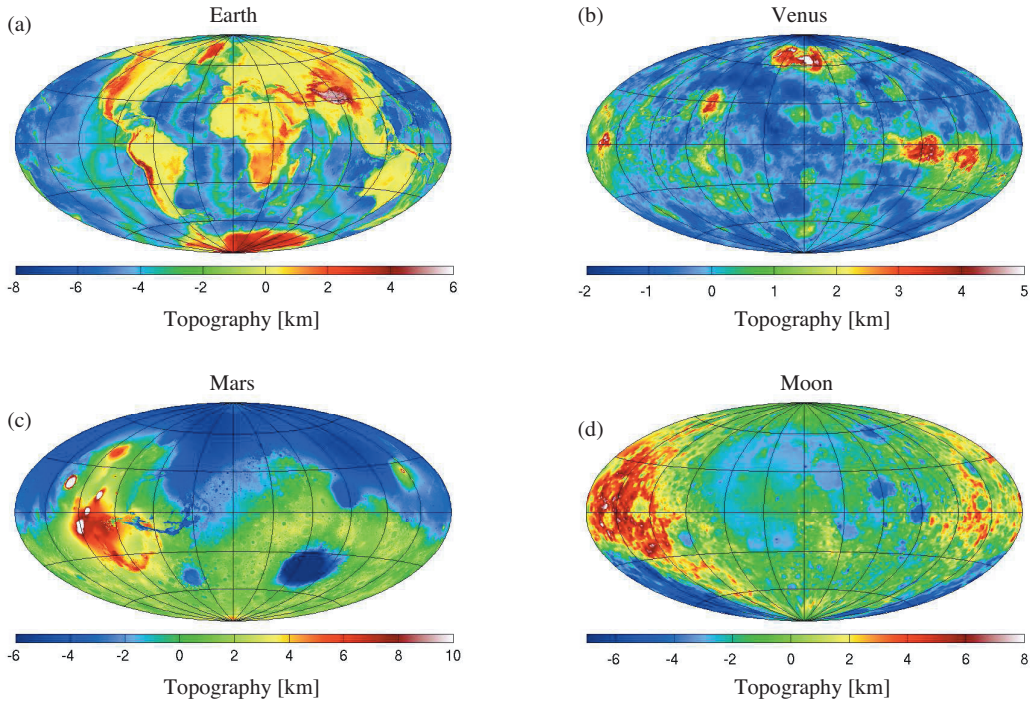

Fig. 4. Topography of (a) the Earth, (b) Venus, (c) Mars and (d) the Moon as derived from the topographic models given in Table 8. All images are in a Hammer projection with a central meridian of 0° W. Zero elevation is given by (a) the mean sea level, (b) a sphere of 6051.8 km radius, (c) the gravitational equipotential surface whose average radius at the equator is equal to the mean equatorial radius of 3396 km and (d) a spheroid with an equatorial radius of 1738 km and a flattening of 1/3234.93.

4.2.3.4 Dynamics and thermal evolution

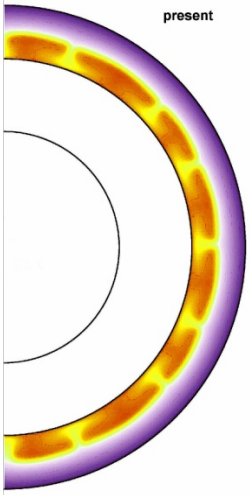

Fig 2. A typical temperature field of the convecting mantle (coloured region) in Mercury calculated with a 2D axisymmeteric convection model with strongly temperature and pressure dependent viscosity. The temperature decreases from brownish colours to yellow, violet, and blue. The upper violet to blue part is the stagnant lid, convection takes place underneath. The solid circle in the center indicates the present size of the inner core. The viscosity increases by a factor of 10 in the convecting mantle and by 5 orders of magnitude in this model of the lid. The model assumes a concentration of radioactive heat sources consistent with the silicate vaporization model [87Feg] and a concentration of 1 wight-% sulfur in the core [after 99Con].

4.2.3.5 Planetary geology

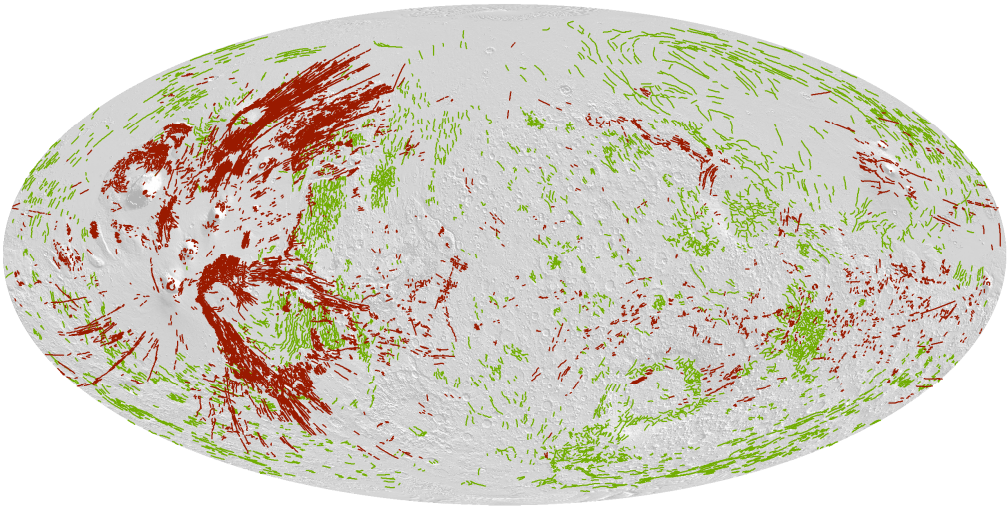

Fig. 16. Global tectonic map of Mars (Mollweide projection centered at 0° longitude) [06Kna]. Red lines mark extensional faults (normal faults, grabens, rifts), green lines mark contractional features (thrust faults, wrinkle ridges). The majority of faults are associated with the largest volcano-tectonic province on Mars, Tharsis, in the western hemisphere.

4.2.3.6 Planetary photometry and spectroscopy

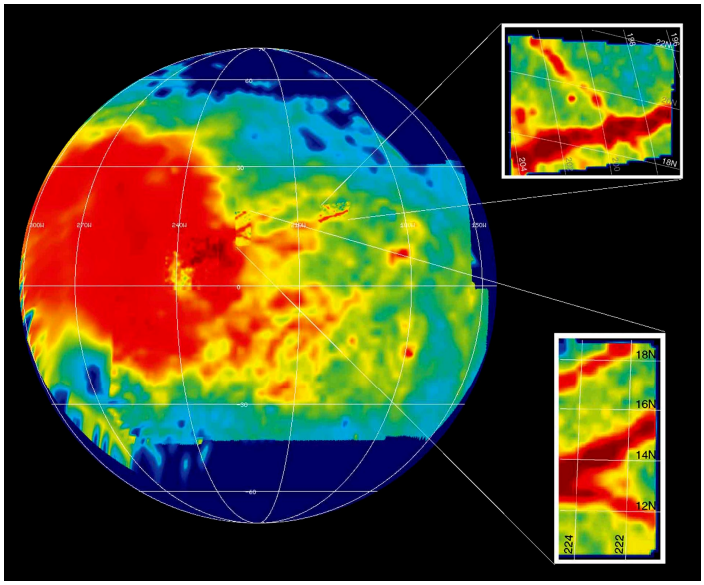

Fig. 9. Distribution of hydrated minerals on Europa [98McC, 99McC].

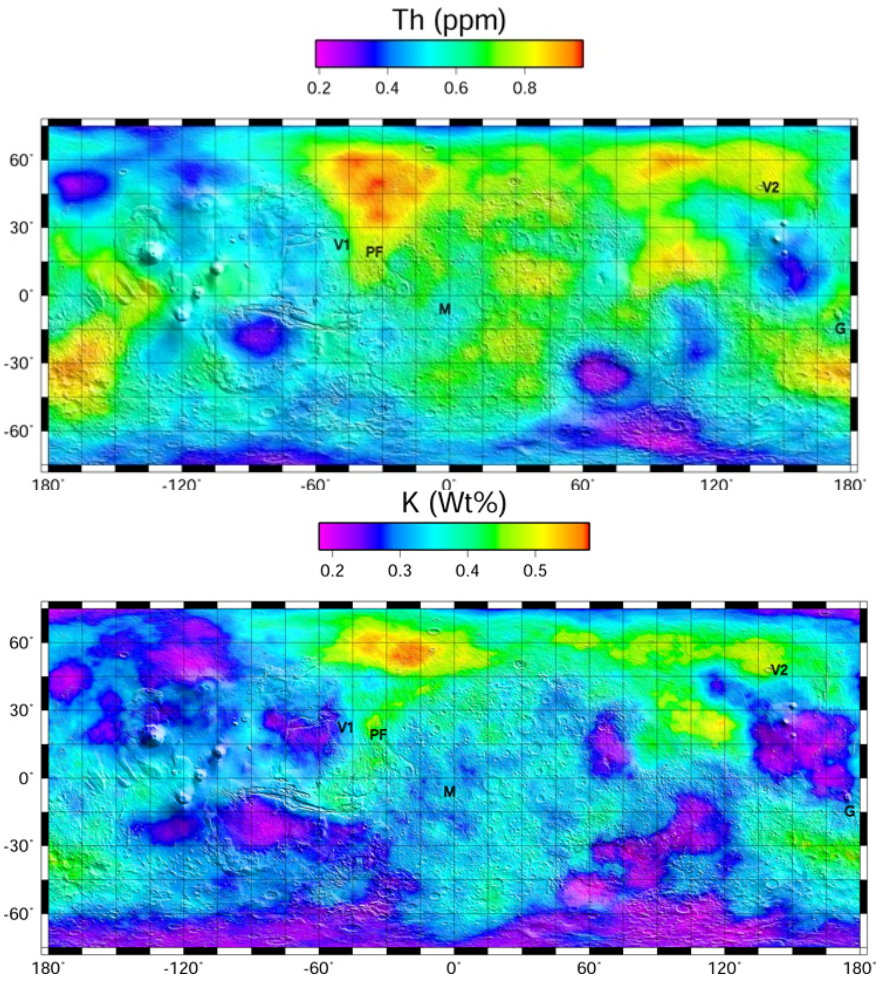

Fig. 11. Maps of the distribution of K and Th on Mars, as measured by the Mars Odyssey gamma-ray spectrometer. Data have been smoothed using a 10 by 10 pixel boxcar filter. The data are displayed over a shaded relief map of Mars, with mission landing sites indicated: V1 and V2, Viking 1 and 2; PF, Pathfinder; M, Opportunity in Meridiani Planum; G, Spirit in Gusev Crater [06Tay].

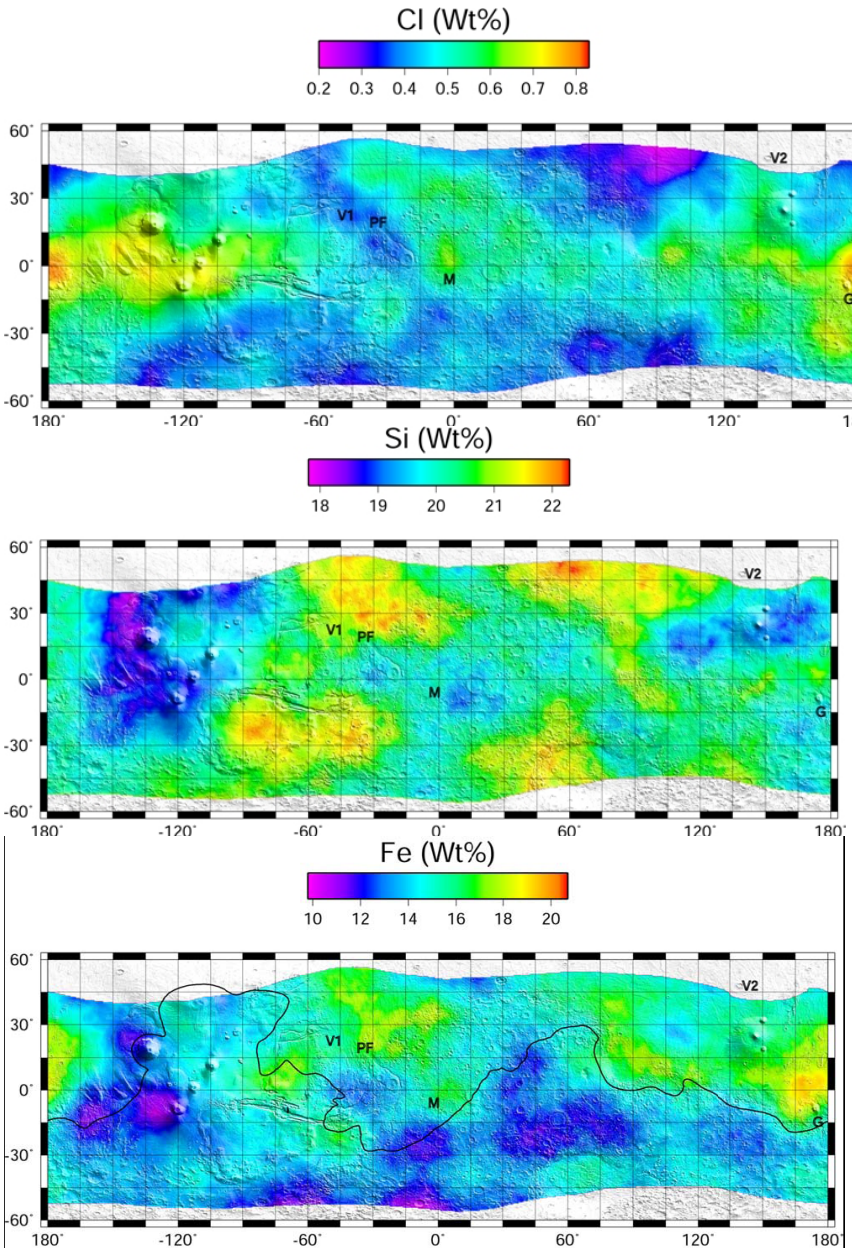

Fig 12. Map of the distribution of Cl, Si, and Fe on Mars as measured by the Mars Odyssey gamma-ray spectrometer. Data have been smoothed using a 10 by 10 pixel boxcar filter. The mapped area encompasses only hat portion of Mars in which H content does not dominate. The data are displayed over a shaded relief map of Mars, with mission landing sites indicated: V1 and V2, Viking 1 and 2; PF, Pathfinder; M, Opportunity in Meridiani Planum; G, Spirit in Gusev Crater. The black line represents the 0-km contour, a reasonable separation between highlands and lowlands [06Tay].

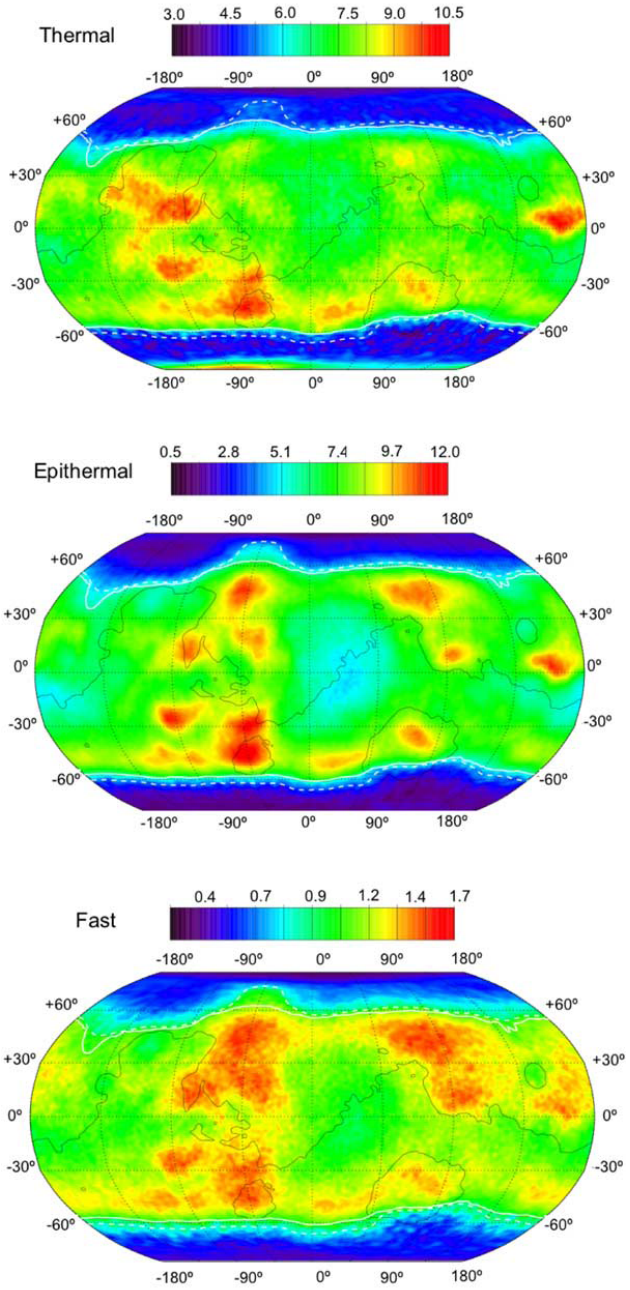

Fig. 13. Thermal, epithermal, and fast neutron CO_2 frost-free maps of Mars. Data north of the northern white dashed wavy line were measured after the northern summer solstice ($100 < Ls < 151$), and data south of the southern dashed wavy line were measured during the late summer in the south ($329 < Ls < 1.7$). The 0-km elevation contour (black line) is included for reference. The solid white lines separate the poleward regions having water abundances larger than about 11% by mass from those at near equatorial latitudes that have abundances that are less than 11% [02Fel].

4.2.3.8 Magnetic fields

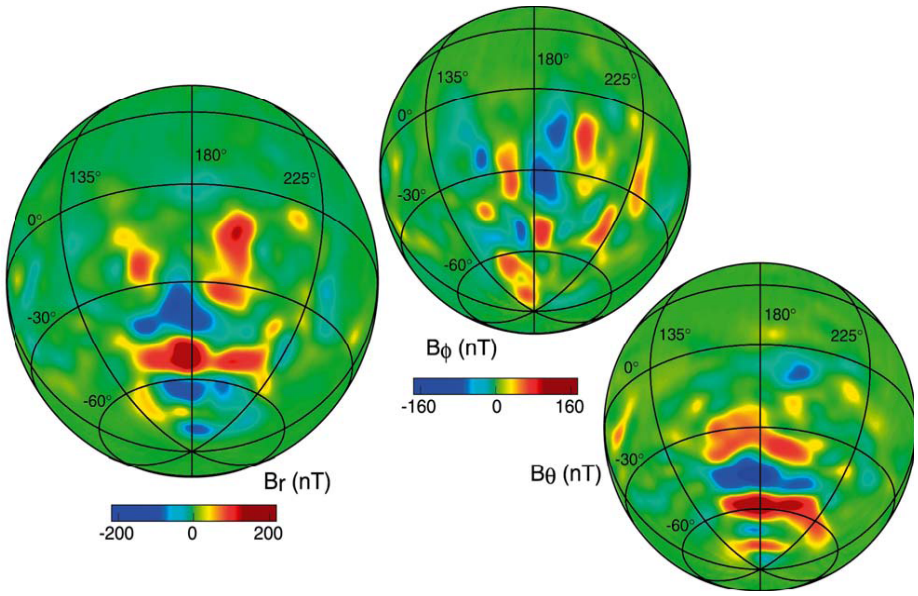

Fig. 1. Orthographic projections of the three components of the magnetic field (B_r , B_θ , B_Φ) at a nominal 400 km mapping orbit altitude, viewed from 30 deg S and 180 deg East longitude (from [04Con]). © Springer Verlag

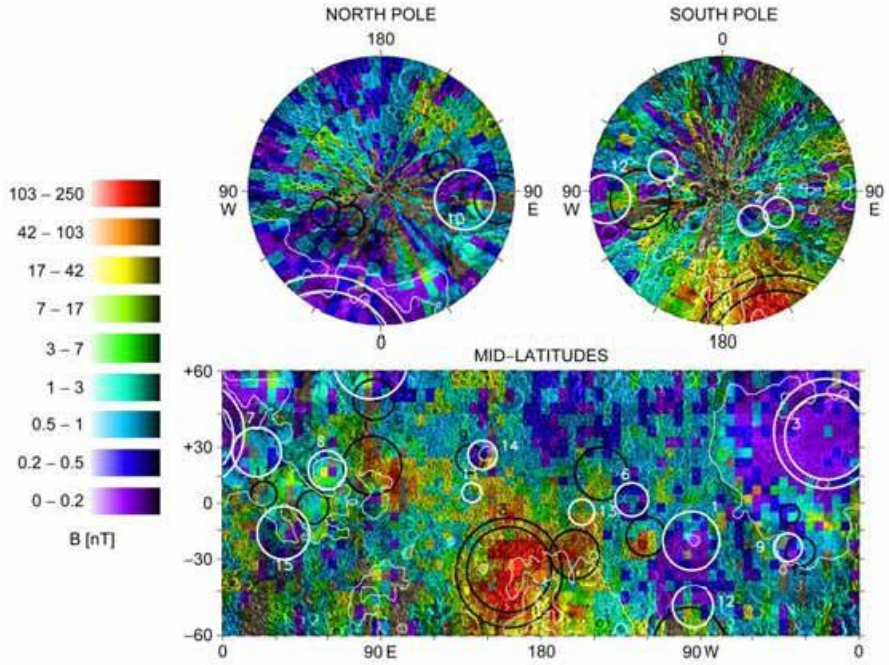

Fig. 2. Magnetic field at the surface of the Moon measured by the electron refelction experiment on Lunar Prospector in orthographic projection (from [07Mit]). The white circles indicate major impact basins and the black circles their antipodal regions. © American Geophysical Union

4.3.2 Meteors

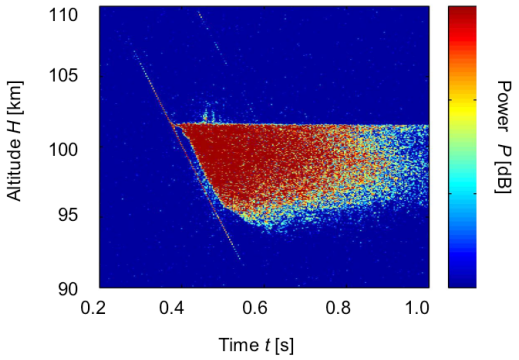

Fig. 2. (a) The intensity of a meteor radar signal as function of time and altitude measured with the ALTAIR VHF radar (160 MHz) [07Clo]. The diagonal line at the left is the head echo signal, while the signal on the right of this line that extends in altitude and time is the non-specular trail signal.

4.3 Small bodies in the Solar System

4.3.5 Interplanetary dust

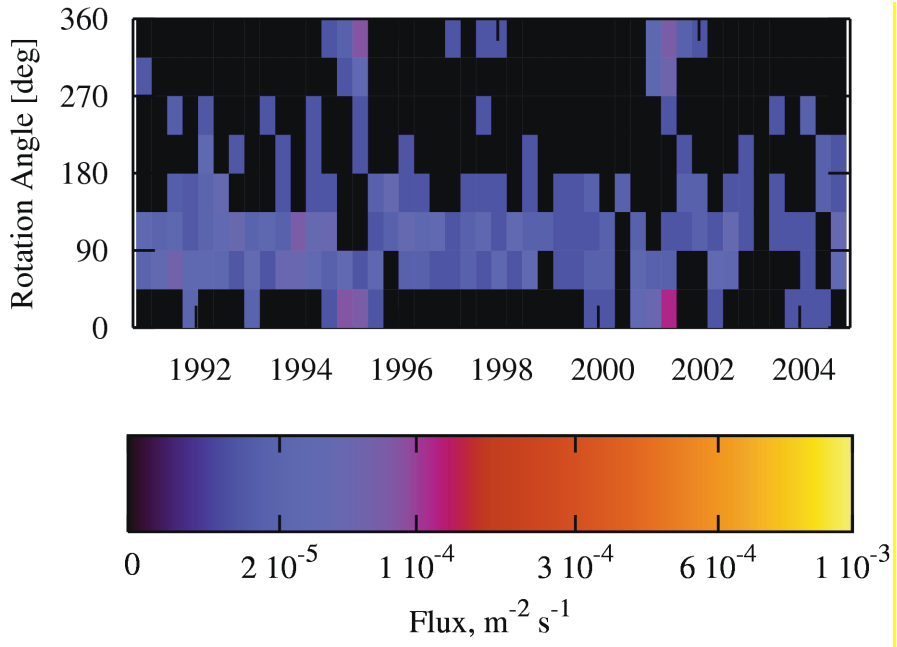

Fig. 11. Meteoroid fluxes measured by the Ulysses dust detector, as a function of mission time and detector orientation [G13, K16]. The rotation angle is the azimuth of the detector pointing axis measured from its ecliptic northern culmination. Selected are impacts by meteoroids bigger than ≈ 10-13 g at the velocity of 20 km s^{-1}.

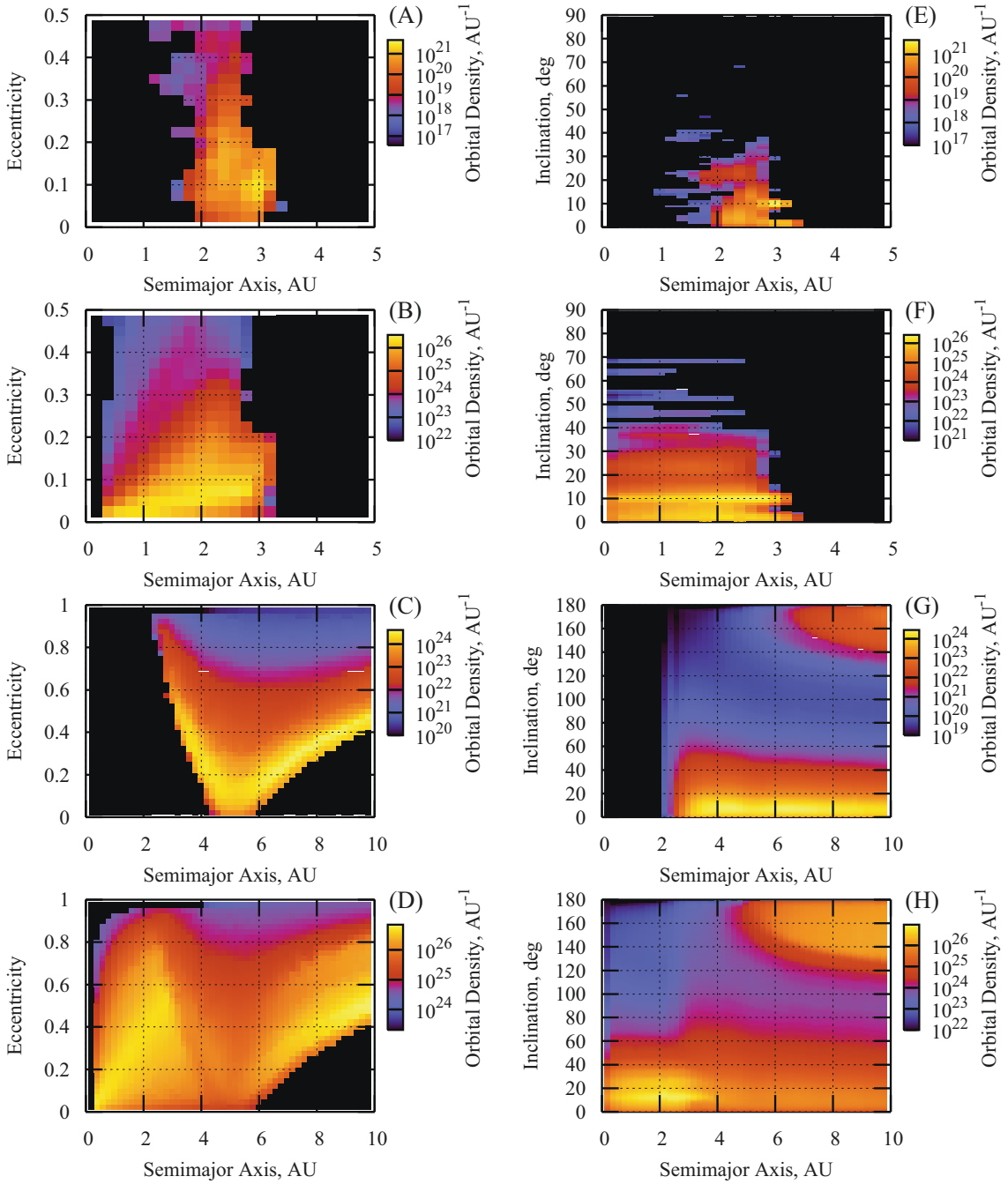

Fig. 15. Orbital distributions of interplanetary dust particles in the ESA meteoroid model [05Dik], calculated for the minimum mass threshold 10 - 12 g. They can be multiplied by the mass distributions in Fig. 14 to obtain the absolute numbers of particles above any other mass covered by the model. The left column shows the distribution in semimajor axis and eccentricity, the right column shows the distribution in semimajor axis and inclination. Four distinct populations are shown. Plots A and E: the big dust particles ($m > 10^{-5}$ g) from asteroids in collisional regime. Plots C and G are the same for comets in Jupiter-crossing orbits. Plots B and F: small dust grains (mass $m < 10^{-5}$ g) from asteroids, spiraling toward the Sun under the Poynting-Robertson effect. Plots D and H are the same for comets.

4.3.6 Interplanetary particles and magnetic fields

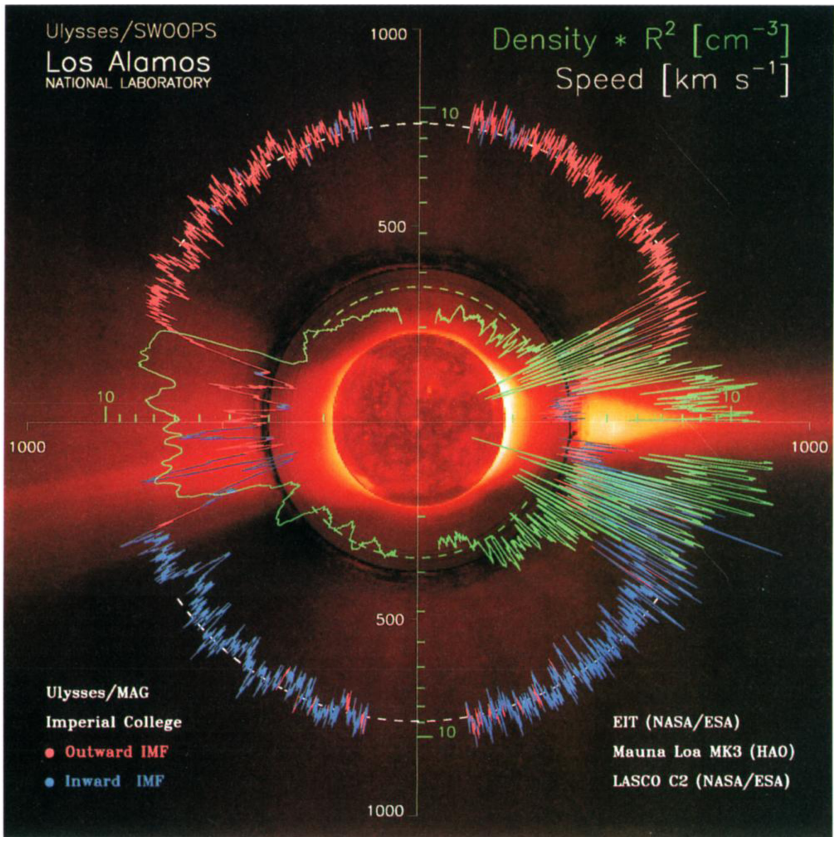

Fig. 1. Summary plot of the first orbit of Ulysses over the poles of the Sun. The solar wind proton density (green trace) shows a one solar rotation running average. The red and blue traces show one hour averages of the solar wind speed for outward (red) and inward (blue) interplanetary magnetic field, respectively [00M].